Lawrence Berkeley National Laboratory

LBL Publications

Title

Hardness and microstructural inhomogeneity at the epitaxial interface of laser 3D-printed Ni-based superalloy

Permalink

https://escholarship.org/uc/item/9778202q

Journal

Applied Physics Letters, 109(10)

ISSN

0003-6951

Authors

Qian, Dan
Zhang, Anfeng
Zhu, Jianxue
et al.

Publication Date

2016-09-05

DOI

10.1063/1.4962485

Peer reviewed

eScholarship.org Powered by the California Digital Library
University of California

Hardness and microstructural inhomogeneity at the epitaxial interface of laser 3D-printed Ni-based superalloy

Dan Qian[1], Anfeng Zhang[2], Jianxue Zhu[1], Yao Li[1], Wenxin Zhu[1], Baolu Qi[2], Nobumichi Tamura[3], Dichen Li[2], Zhongxiao Song[1], Kai Chen[1 *]

1. State Key Laboratory for Mechanical Behavior of Materials, Xi'an Jiaotong University, Xi'an, Shaanxi 710049, China
2. State Key Laboratory for Manufacturing Systems Engineering, Xi'an Jiaotong University, Xi'an, Shaanxi 710049, China
3. Advanced Light Source, Lawrence Berkeley National Laboratory, Berkeley, CA 94720, USA

Correspondence and requests for materials should be addressed to K.C. (kchenlbl@gmail.com)

Abstract

In this Letter, microstructural and mechanical inhomogeneities, a great concern for single crystal Ni-based superalloys repaired by laser assisted 3D printing, have been probed near the epitaxial interface. Nanoindentation tests show the hardness to be uniformly lower in the bulk of the substrate and constantly higher in the epitaxial cladding layer. A gradient of hardness through the heat affected zone is also observed, resulting from an increase in dislocation density, as indicated by the broadening of the synchrotron X-ray Laue microdiffraction reflections. The hardening mechanism of the cladding region, on the other hand, is shown to originate not only from high dislocation density, but also and more importantly from the fine γ/γ' microstructure.

KEYWORDS: Hardness and microstructural inhomogeneity, Laser assisted 3D printing, Ni-based superalloy, Synchrotron X-ray microdiffraction, Interface

The possibility of preserving the single crystalline nature of Ni-based superalloy endows laser 3D-printing with high promise in repairing aero-engine components, prolonging their service lifetime, and reducing cost.[1] Because of the high solidification rates inherent to this technique, finer columnar dendrites grow in epitaxy with the substrate to form a metallurgical interface. The epitaxy is lost after a few laser passes and equiaxed stray grains with random orientation start to grow.[2, 3] The columnar-to-equiaxed transition has been studied extensively since the high-angle grain boundaries (HAGBs) between stray grains provide easy paths for crack initiation and propagation.[4, 5] In recent works, defect density in the epitaxial layer is found to be significantly higher than in the substrate and to increase as the cladding layer deposits.[6, 7] Concerns regarding the mechanical properties are therefore raised from such inhomogeneous microstructure: How and why does the mechanical property change from the substrate to the cladding layer? Does the mechanical property in the cladding layer vary as a function of defect density? These questions are of great importance for the development and application of the laser 3D-printing technique to repair single crystalline Ni-based superalloy. Here we probe the mechanism of the hardness increase near the epitaxial interface in laser 3D-printed DZ125L Ni-based superalloy by combining nanoindentation and synchrotron X-ray Laue microdiffraction (μXRD) measurements, which proved to be an efficient method for correlating mechanical with structural information at the micron scale.[8]

The 3D-printing experiment was conducted on an independently developed system equipped with a Nd:YAG laser under the parameters listed in Table 1.[9] As shown in Fig. 1a, a Cartesian coordinate system **O-XYZ** was established, with **X**-axis parallel to the laser scanning direction and **Y**-axis perpendicular to the cladding-substrate interface. DZ125L superalloy powders with 50-100 μm diameter particles, protected in high purity argon atmosphere, were injected coaxially into the laser heating generated molten pool on the {100} crystal plane of a directionally solidified DZ125L substrate. By unidirectional single channel scan, a 10-layer high, ~0.8 mm thick sample was formed. Between each two successive layers, the sample was moved by 0.1 mm vertically, defining the height of each layer.

Nanoindentation tests were performed in the interfacial area on **XY** plane at room temperature, indicated by the red triangles array in Fig. 1a. Using a TI950 TriboIndenter (Hysitron, Minneapolis, MN) with a standard Berkovich tip, loading-control mode was applied at constant rate of 800 $\mu N \cdot s^{-1}$. The load was held at 4000 μN for 2 s before unloading. A total of 240 indents, distributed in 6 parallel lines along **Y**-axis across the interface, were tested, and the distance between two adjacent indents was 10 μm to prevent the interaction of the plastic zones. The hardness, displayed in Fig. 1b, was obtained from the instrument recorded force-displacement curve applying the Oliver-Pharr method.[10] The hardness is constant at approximately 6.1 ± 0.2 GPa deep into the substrate ($Y < -100$ μm), whereas in the cladding layer it is stable all over the measured 200 μm length range ($Y > 0$), at about 7.4 ± 0.3 GPa, 21% higher than in the substrate. Within a 100 μm range from deep substrate to interface (-100 μm $< Y < 0$), the hardness increases monotonically. This region is believed to be the heat affected zone (HAZ) formed during the deposition of the first cladding layer.

A 200 μm (horizontal) by 600 μm (vertical) area was studied with μXRD technique on Beamline 12.3.2 at the Advanced Light Source of the Lawrence Berkeley National Laboratory,[11] 400 μm deep into the substrate and 200 μm in the cladding region. With 5 μm scanning step size, 4800 patterns were recorded and analyzed using the software package XMAS[12] to obtain the high angular resolution (~ 0.01°) crystal orientation at each scanning position.[13, 14] From the inverse pole figures along **X**- and **Y**-directions (Fig. 2a and 2b, respectively), the crystal orientation was preserved across the interface (grey dashed line). The columnar dendrites, which grew along **Y**-axis, were parallel to the <100> crystal direction, while the **X**- and **Z**-directions were roughly parallel to the <052> directions, as confirmed from the {100} and {052} pole figures in Fig. 2c and 2d, respectively.

From the analysis of the Laue patterns, no change in precipitate density or HAGBs are observed in the scanned area, while inhomogeneous dislocation density and low-angle grain boundaries (LAGBs) are detected. The distribution of average peak width, which is defined as the average full width at half maximum (FWHM), in degrees, of all recorded reflections in each Laue pattern, is plotted in Fig. 3a. Two sharp boundaries are visible in the map and divide the scanned area into three regions, marked as I to III here. The diffraction peaks in region II are significantly broadened, indicating high density of dislocations.[15] To simplify the analysis, the position and shape of the 115 reflection, close to the center of the detector, is plotted in the Bragg-azimuthal (2θ-χ) space in Fig. 3b and 3c, respectively, as a function of sample position along the vertical dotted line in Fig. 3a. Note that the 2θ map spans a 9° angular range while the χ map spans only 4°. The reflections in region I remain isotropic and sharp, confirming low defect density in the substrate. The broadening is significantly anisotropic in region II, suggesting high density of randomly distributed unpaired geometrically necessary dislocations (GNDs). Subpeaks in region III indicate the formation of geometrically necessary boundaries (GNBs).[16] In other words, the dislocation distribution is negligible in region I, high but random in region

II, while high and inhomogeneous in region III. It is also noted that reflection positions in the Laue patterns unequivocally shift in region II and III, therefore crystal disorientation needs to be taken into account. The disorientation angle between each pair of adjacent scan positions is computed[17] and plotted in Fig. 3d, showing LAGBs (< 1°) in HAZ and cladding layers. The disorientation angles are averaged along each **Y**-coordinate and shown in Fig. 3e. It can be seen that the disorientation angles in region I is lower than 0.1°, while more than three times higher in region III, and have intermediate values in region II.

Since Vickers hardness (H_V) is generally accepted as an empirical linear function of yield strength (σ_s),[18, 19] and Berkovich hardness (H_{Berk}) is linearly related to H_V,[20] we conclude that the nanohardness measured here (H_{Berk}) is linearly proportional to σ_s, and thereby the nanoindentation results can be understood from the well-established strengthening mechanisms. From the von Mises' flow rule, σ_s is linearly related to the shear strength τ, and τ depends in turn on dislocation density:[21]

$$\tau = k\mu b\sqrt{\rho_{total}}\ , \quad (1)$$

where ρ_{total} is the total dislocation density, a summation of GNDs and paired statistically stored dislocations (SSDs), μ the shear modulus, b the Burgers vector and k a linear coefficient. Thus H_{Berk} is also linearly proportional to $\sqrt{\rho_{total}}$:

$$H_{Berk} \propto \sqrt{\rho_{total}}\ . \quad (2)$$

The observed Laue peaks in both region II and III are anisotropically broadened, indicating that unpaired GNDs are dominating,[16] so the total dislocation density ρ_{total} is approximated to be the density of GNDs (ρ_G).

Considering the relationship between crystal plane bending and dislocations, GND density can be quantified by measuring: 1) the characteristic FWHM of streaking peaks in 2θ direction ($\Delta\theta_1$), 2) the disorientation angle between subgrains ($\Delta\theta_2$) for the peaks that are splitting, and 3) the disorientation angle between a pair of adjacent scanning steps ($\Delta\theta_3$), and applying the following equation:[15]

$$\rho_G = \frac{2sin\frac{\Delta\theta}{2}}{Db}, \tag{3}$$

where $\Delta\theta$ is the maximum value among $\Delta\theta_1$, $\Delta\theta_2$, and $\Delta\theta_3$, and D is the length corresponding to the angle $\Delta\theta$, i.e. the diameter of the X-ray probe (D_{beam}) for $\Delta\theta_1$ and $\Delta\theta_2$ and the scanning step size (D_{scan}) for $\Delta\theta_3$. Usually the angle $\Delta\theta$ is small, therefore $sin\frac{\Delta\theta}{2}$ is replaced by $\frac{\Delta\theta}{2}$ in radian, leading to the relation:

$$\rho_G = \frac{1}{b}\cdot \max\left\{\frac{\Delta\theta_1}{D_{beam}}, \frac{\Delta\theta_2}{D_{beam}}, \frac{\Delta\theta_3}{D_{scan}}\right\}. \tag{4}$$

For simplicity, we call the term $\max\left\{\frac{\Delta\theta_1}{D_{beam}}, \frac{\Delta\theta_2}{D_{beam}}, \frac{\Delta\theta_3}{D_{scan}}\right\}$ disorientation gradient and denote it as $\frac{\Delta\theta}{D}$ hereafter. Combining equations (2) and (4), H_{Berk} is linked with the μXRD experimental results as follows:

$$H_{Berk} \propto \sqrt{\frac{\Delta\theta}{D}}. \tag{5}$$

All three possible disorientation gradient components are calculated and shown in Figure S1 of the supplementary online information (SOI).[23] In most cases $\frac{\Delta\theta_1}{D_{beam}}$ overwhelms the other two terms. The square root of the disorientation gradient

($\sqrt{\frac{\Delta\theta}{D}}$) is plotted in Fig. 4a as hollow circles, and the average values over each **Y**-coordinate are displayed as solid circles. It shows that the disorientation gradient is low in region I, but start to increase prior to HAZ until reaching a maximum value at about 50 μm below the interface, and then start to drop. The measured hardness, however, increases monotonically in HAZ. We attribute the discrepancy to the different probing depths between μXRD and nanoindentation. The 5-24 keV X-ray beam can penetrate the specimen by up to 40 μm, and incident angle is 45°, while the nanoindentation results reflect the hardness of the specimen of only 0.1-0.2 μm in depth. More detailed explanation is shown in Figure S2 in SOI.[22] To avoid the ambiguity of depth penetration, the verification of equation (5) is checked only in the region between the two arrows in Fig. 4a. The linear dependence of H_{Berk} against $\sqrt{\frac{\Delta\theta}{D}}$ (Fig. 4b) is strongly evident and the hardening in HAZ is mainly attributed to the high density of dislocations when the molten pool solidifies rapidly during 3D-printing, and *in situ* thermal annealing may be an effective approach to reduce such inhomogeneity.

In the epitaxial layer, the dislocation density is about 70% higher than in the substrate, which results in hardness increase of no more than 5%. However, from experimental measurement, the hardness in the cladding layer is 21% higher than in the substrate, therefore additional strengthening mechanisms must be operating in this region. Several possible factors, such as residual stress, chemical inhomogeneity, and dendrite size and structure, have been excluded after prudent analysis provided in SOI.[22] From the scanning electron micrographs of the nitro-hydrochloric acid etched sample (Fig. 4c and 4e), the γ’ phase in the substrate show regularly dispersed cubic morphology, while they are much more irregular in the laser cladding zone. A measurement of over 200 γ' particles or cubes in each zone show that the γ' particle size in the cladding layer averages to about 35-40 nm, compared to approximately 400-500 nm in the substrate (Fig. 4d and 4f, respectively), due to the significantly higher temperature gradient and faster solidification rate in 3D-printing process than in traditional casting.[23, 24] It is worth mentioning that the shape and size of the γ' phase in HAZ are similar to the ones in the deep substrate. According to previous reports, the density of interphase interfaces has a great impact on the mechanical behaviors of Ni-based superalloys.[25, 26] Complex nonlinear effects of γ' size on the yield strength of <001> oriented Ni-base superalloy have been reported by Shah *et al*.[27] The room temperature yield strength is reported to be 970 MPa when γ' size is similar to our case (~0.5 μm), and increases to 1080 MPa as γ' shrinks to 0.3 μm. Although no data is available for smaller γ' sizes, it is proposed that the strength limitation is 1167 MPa in the <001> direction. Thus, due to the increase of the interphase boundaries, the yield strength of the cladding layer of our specimen can be estimated to range between 1080 and 1167 MPa, corresponding to an increase of 11% to 20% compared to the substrate. In this reference article, it is not stated whether dislocation strengthening is considered. Since the dislocation density will either stay constant or increase as γ' becomes finer, it is reasonable to estimate that the yield strength will increase by 11% - 25%, which agrees well with the observed 21% increment of H_{Berk} in region III compared to the substrate.

In summary, the inhomogeneous hardness and microstructural distribution is characterized quantitatively in the region near the epitaxial interface of laser 3D-printed single crystal Ni-based superalloy DZ125L. The nanoindentation profile shows three distinct regions along the cladding direction. In the investigated sample, the regions with the constant 6.1 GPa and 7.4 GPa hardness magnitudes correspond to the substrate and epitaxial cladding zone, respectively. Between them a 100 μm thick HAZ is detected, within which the hardness increases monotonically from the substrate to the cladding layer. The hardening mechanisms in the HAZ and epitaxial region are found to be different. From the quantitative analysis of peak shape and disorientation gradient from the μXRD data, it is found that the hardness in HAZ is almost linearly related to the square root of dislocation density, proving that the hardening/strengthening mechanism there results mainly from the high density of dislocations. In the epitaxial region, a quasi-quantitative estimation suggests that the fine γ/γ' microstructure and dense interphase interfaces contribute more to the hardness increment than the high density of dislocations. Although the magnitude of hardness change and HAZ thickness are influenced by the 3D-printing parameters, the trend of hardening is believed to be representative and typical, and the hardening mechanisms unraveled here will shed light on the reliability evaluation and parameter selection of the laser 3D-printing repairing technique.

Acknowledgements

This work is supported by the National Natural Science Foundation of China (Grant No. 51302207, 51275392, 11132006), the National Key Research and Development Program (Grant No. 2016YFB0700404), the National Basic Research Program of China ("973" Program) (Grant No. 2015CB057400), and the Fundamental Research Funds for the Central Universities (Grant No. 2015gjhz03). We also appreciate the support from the International Joint Laboratory for Micro/Nano Manufacturing and

Measurement Technologies and Collaborative Innovation Center of High-End Manufacturing Equipment. KC is supported by the National Young 1000 Talents Program of China. The ALS is supported by the Director, Office of Science, Office of Basic Energy Sciences, Materials Science Division, of the U.S. Department of Energy under Contract No. DE-AC02-05CH11231 at LBNL.

References

[1] R. Vilar, and A. Almeida, *J. Laser Appl.* **27**, S17004 (2015).

[2] M.Gaumann, C. Bezencon, P. Canalis, and W. Kurz, *Acta Mater.* **49**, 1051 (2001).

[3] P. Nie, O. A. Ojo, and Z. Li, *Acta Mater.* **77**, 85 (2014).

[4] Z. Y. Liu, and H. Qi, *J. Mater. Process Tech.* **216**, 19 (2015).

[5] L. Wang, N. Wang, W. J. Yao, and Y. P. Zheng, *Acta Mater.* **88**, 283 (2015).

[6] Y. Li, D. Qian, J. W. Xue, J. C. Wan, A. F. Zhang, N. Tamura, Z. X. Song, K. Chen, Ap*pl. Phys. Lett.* **107**, 181902 (2015).

[7] J. W. Xue, A. F. Zhang, Y. Li, D. Qian, J. C. Wan, B. L. Qi, N. Tamura, Z. X. Song, K. Chen, *Sci. Rep.* **5**, 14903 (2015).

[8] A. Lupinacci, K. Chen, Y. Li, M. Kunz, Z. Jiao, G. S. Was, M. D. Abad, A. M. Minor, P. J. Hosemann, *J. Nucl. Mater.* **458**, 70 (2015).

[9] X. Do, D. C. Li, A. F. Zhang, B. He, H. Zhang, and T. Doan, *J. Laser Appl.* 25, 012007 (2013).

[10] W. C. Oliver, and G. M. Pharr, *J. Mater. Res.* **7**, 1564 (1992).

[11] M. Kunz, N. Tamura, K. Chen, A. A. MacDowell, R. S. Celestre, M. M. Church, S.

Fakra, E. E. Domning, J. M. Glossinger, J. L. Kirschman, G. Y. Morrison, D. W. Plate, B. V. Smith, T. Warwick, V. V. Yashchuk, H. A. Padmore, E. Ustundag, *Rev. Sci. Instrum.* **80**, 035108 (2009).

[12] N. Tamura, in *Strain and Dislocation Gradients from Diffraction Spatially Resolved Local Structure and Defects*, edited by R. Barabash and G. Ice (World Scientific, London, 2014), pp. 125-155.

[13] K. Chen, N. Tamura, W. Tang, M. Kunz, Y. C. Chou, K. N. Tu, and Y. S. Lai, *J. Appl. Phys.* **107**, 063502 (2010).

[14] K. Chen, M. Kunz, N. Tamura, and H.-R. Wenk, *Geology* **43**, 219 (2015).

[15] R. I. Barabash, , G. E. Ice, and F. J. Walker, *J. Appl. Phys.* **93**, 1457 (2003).

[16] G. E. Ice, and R. I. Barabash, in *Dislocations in Solids*, edited by F. R. N. Nabarro, and J. P. Hirth, Elsevier (2007), pp. 499-601.

[17] Y. Li, L. Wan, and K. Chen, *J. Appl. Crystallogr.* **48**, 747 (2015).

[18] W. D. Nix, and H. Gao, *J. Mech. Phys. Solids* **46**, 411 (1998).

[19] P. Zhang, , S. X. Li, and Z. F. Zhang, *Mater. Sci. Eng., A* **529**, 62 (2011).

[20] J. G. Swadener, , E. P. George, and G. M. Pharr, *J. Mech. Phys. Solids* **50**, 681 (2002).

[21] R. Rodriguez, and I. Gutierrez, *Mater. Sci. Eng., A* **361**, 377 (2003).

[22] See supplemental material at [URL inserted by AIP] for the distribition of disorientation gradient components, explanation for the position discrepancy between the hardness and the disorientation gradient profiles, elements distribution, and metallographic image in Figure S1, S2, S3, and S4, respectively.

[23] J. C. Lippold, S. D. Kiser, and J. N. DuPont, *Welding metallurgy and weldability of nickel-base alloys*. John Wiley and Sons (2011), pp. 175-182.

[24] Y. Zhang, Y. Huang, , Yang, L. and J. Li, *J. Alloys Compd.* **570**, 70 (2013).

[25] B. Reppich, *Acta Metall.* **30**, 87 (1982).

[26] H. Bian, X. Xu, Y. Li, Y. Koizumi, Z. Wang, M. Chen, K. Yamanaka, and A. Chiba, *NPG Asia Mater.* **7(8)**, e212 (2015).

[27] D. M. Shah, and D. N. Duhl, in *The fifth international symposium on superalloys, Metals Park, Ohio*. ASM (1984).

Table 1. Technical parameters employed in the laser assisted 3D printing process

Parameter	Value	Parameter	Value
Laser power (W)	230	Powder feed rate (mm^3/s)	8
Scanning rate (mm/s)	8	Carrying gas injection rate (L/min)	4
Beam diameter (mm)	~0.5	**Y**-increment (mm)	0.1

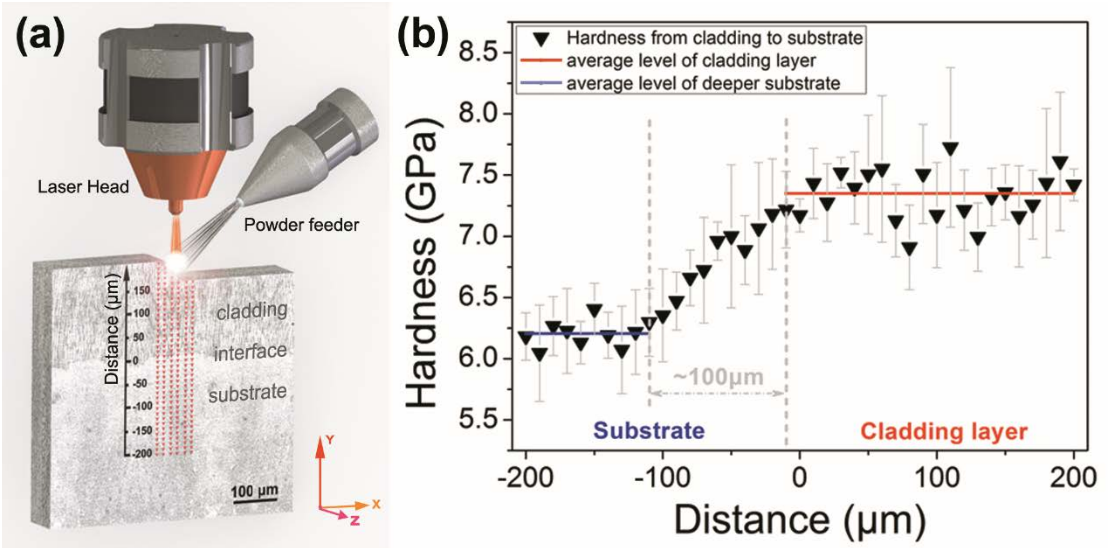
(a)
Laser Head
Powder feeder
Distance (μm)
150
100
50
0
-50
-100
-150
-200
cladding
interface
substrate
Y
X
Z
100 μm
(b)
Hardness from cladding to substrate
average level of cladding layer
average level of deeper substrate
Hardness (GPa)
8.5
8.0
7.5
7.0
6.5
6.0
5.5
~100μm
Substrate
Cladding layer
-200
-100
0
100
200
Distance (μm)

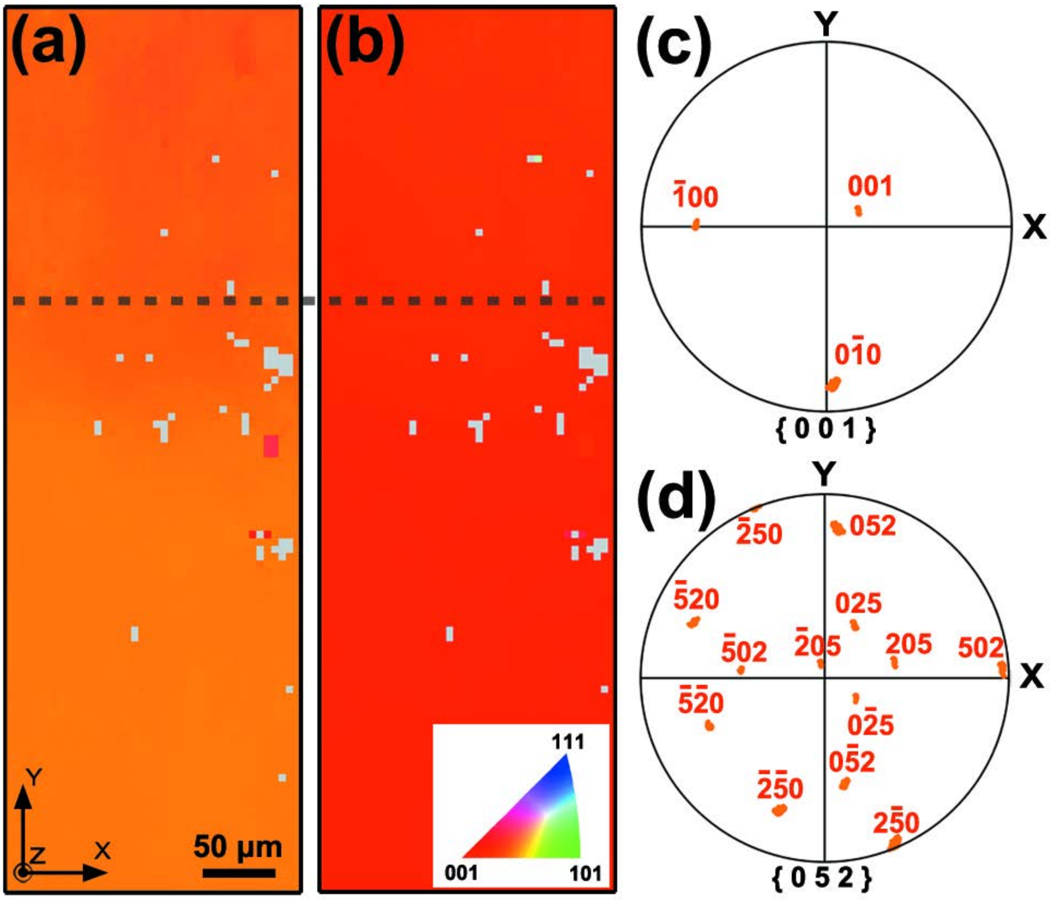

(a)
(b)
(c)
(d)
Y
X
Z
50 μm
111
001
101
$\bar{1}00$
001
$0\bar{1}0$
{ 0 0 1 }
$\bar{2}50$
052
$\bar{5}20$
025
$\bar{5}02$
$\bar{2}05$
205
502
$\bar{5}\bar{2}0$
$0\bar{2}5$
$0\bar{5}2$
$\bar{2}\bar{5}0$
$2\bar{5}0$
{ 0 5 2 }

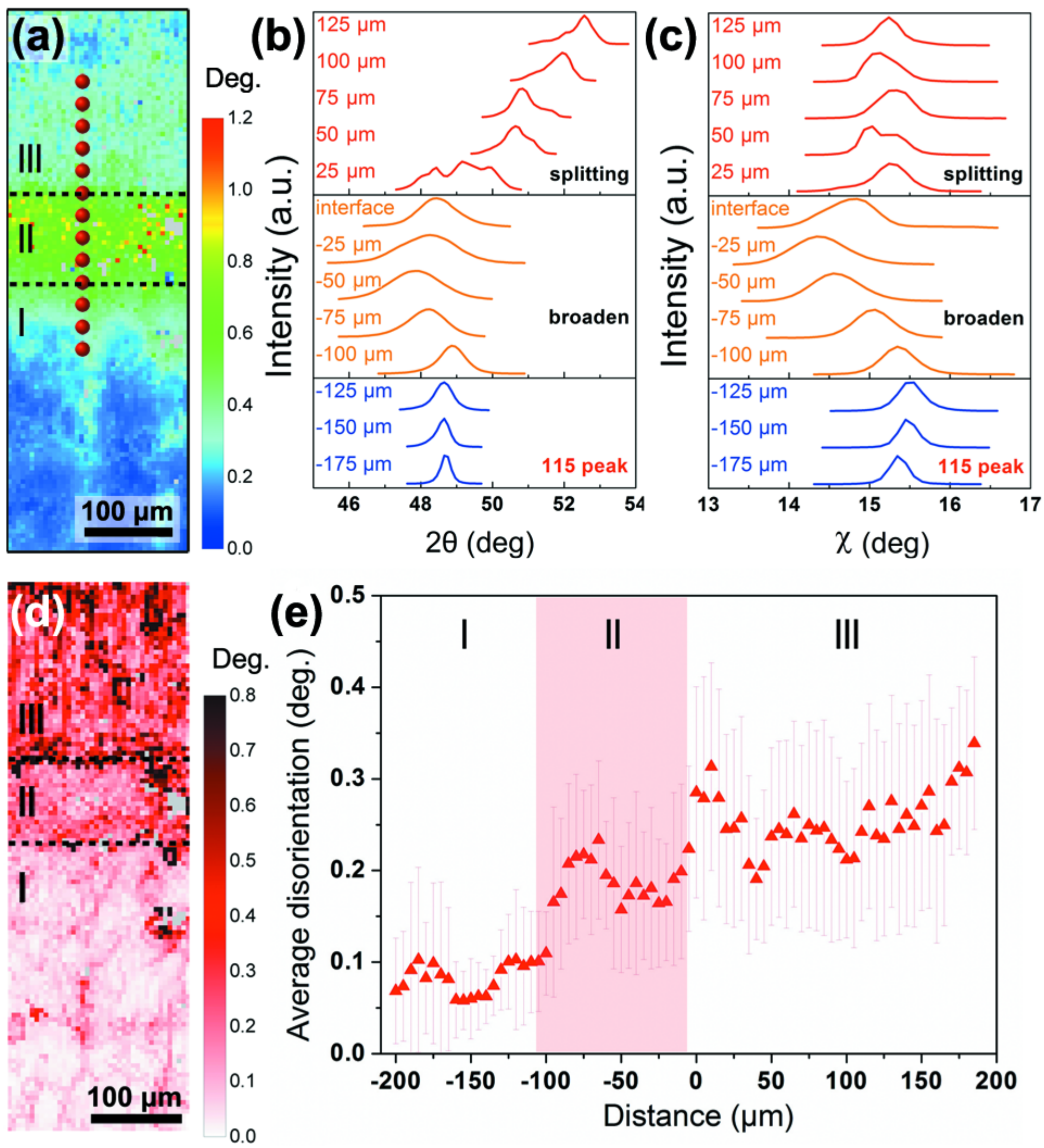

(a)
Deg.
1.2
1.0
0.8
0.6
0.4
0.2
0.0
III
II
I
100 μm
(b)
125 μm
100 μm
75 μm
50 μm
25 μm
splitting
interface
-25 μm
-50 μm
-75 μm
-100 μm
broaden
-125 μm
-150 μm
-175 μm
115 peak
Intensity (a.u.)
46
48
50
52
54
2θ (deg)
(c)
125 μm
100 μm
75 μm
50 μm
25 μm
splitting
interface
-25 μm
-50 μm
-75 μm
-100 μm
broaden
-125 μm
-150 μm
-175 μm
115 peak
Intensity (a.u.)
13
14
15
16
17
χ (deg)
(d)
Deg.
0.8
0.7
0.6
0.5
0.4
0.3
0.2
0.1
0.0
III
II
I
100 μm
(e)
I
II
III
Average disorientation (deg.)
0.0
0.1
0.2
0.3
0.4
0.5
-200
-150
-100
-50
0
50
100
150
200
Distance (μm)

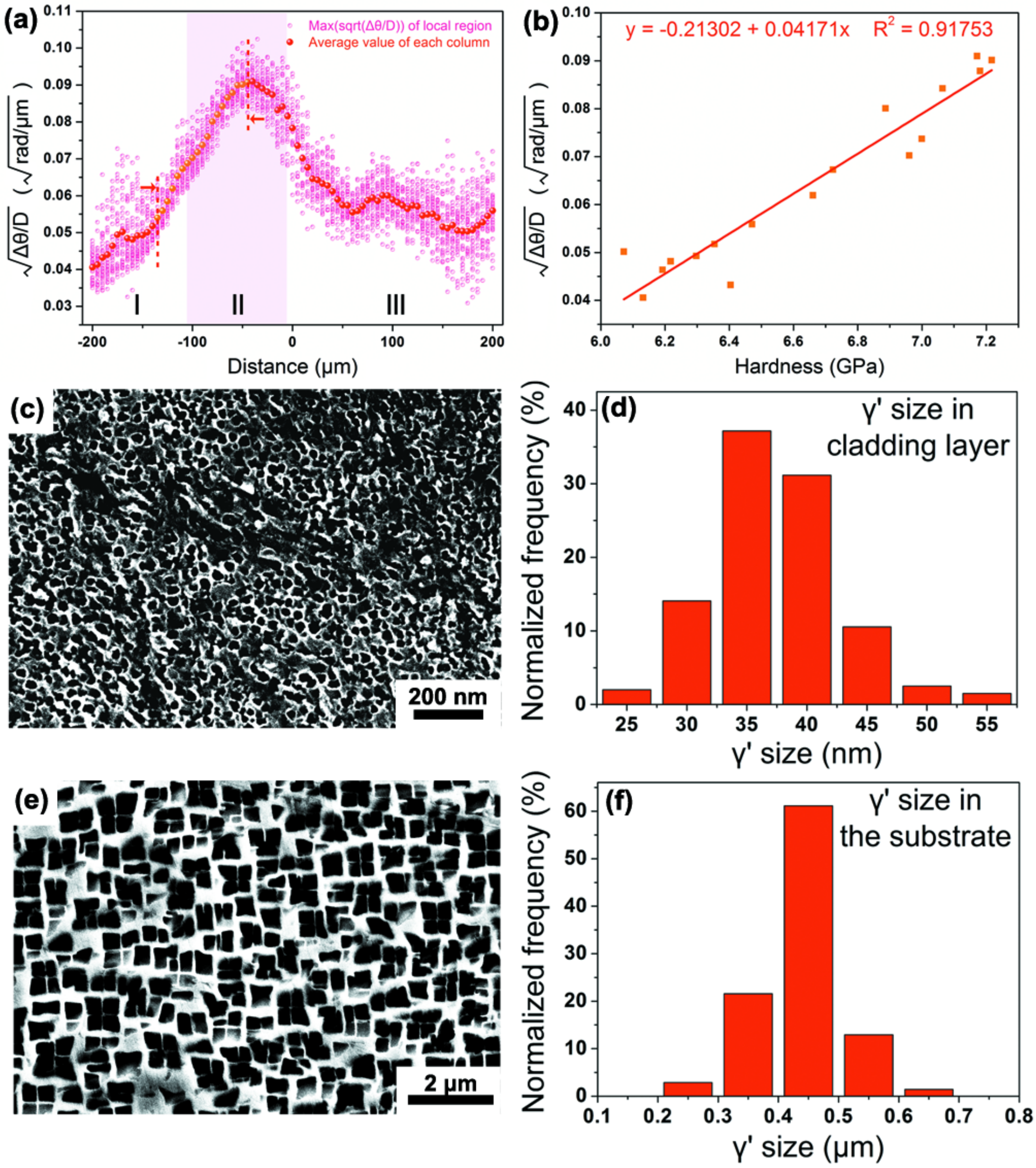
(a)
Max(sqrt(Δθ/D)) of local region
Average value of each column
$\sqrt{\Delta\theta/D}$ ($\sqrt{rad/\mu m}$)
I
II
III
Distance (μm)
(b)
y = -0.21302 + 0.04171x R² = 0.91753
$\sqrt{\Delta\theta/D}$ ($\sqrt{rad/\mu m}$)
Hardness (GPa)
(c)
200 nm
(d)
γ' size in
cladding layer
Normalized frequency (%)
γ' size (nm)
(e)
2 μm
(f)
γ' size in
the substrate
Normalized frequency (%)
γ' size (μm)

274

Figure legends

FIG. 1 (a) Laser 3D-printing experimental setup and an optical micrograph of the specimen, showing the nanoindentation distribution (in red) of the interested region. (b) Nanohardness results as a function of the distance from substrate to cladding.

FIG. 2 (a-b) Orientation maps of the in-plane X- and Y-directions, respectively, from μXRD characterization. (c-d) {001} and {052} stereographic projection figures.

FIG. 3 (a) Average peak width distribution of the scanned area. (b-c) Position and width of 115 peak in 2θ and χ directions, respectively, as a function of **Y**-coordinate. (d) Map of disorientation angle between each pair of adjacent scanning positions. (e) Distribution of disorientation angle averaged over each **Y**-position.

FIG. 4 (a) Averaged square root of disorientation gradient and (b) its relationship with measured nanohardness. Morphology of the γ/γ' microstructure of the cladding region (c) and substrate (e) is observed in SEM, and the size distribution of the γ' phase is studied statistically in each region (d, f).